# Scanning microwave microscopy/spectroscopy on metal-oxide-semiconductor systems

J. Smoliner,[1,a)] H. P. Huber,[2] M. Hochleitner,[2] M. Moertelmaier,[3] and F. Kienberger[3]
[1]*Institut für Festkörperelektronik, TU-Wien, Floragasse 7, 1040 Wien, Austria*
[2]*Christian Doppler Laboratory for Nanoscopic Methods in Biophysics, University of Linz, Altenbergerstrasse 69, 4040 Linz, Austria*
[3]*Agilent Technologies Österreich GmbH, Aubrunnerweg 11, 4040 Linz, Austria*

(Received 25 June 2010; accepted 26 July 2010; published online 22 September 2010)

In this paper, an analytical model for capacitance measurements by scanning microwave microscopy (SMM)/scanning microwave spectroscopy is presented. The tip-sample interactions are included by using the physics of metal-oxide-semiconductor junctions and the influence of various experimental parameters, such as the operation frequency, tip bias, tip area, oxide thickness, and sample doping are discussed. For calibrated carrier profiling it is shown that all relevant operation parameters of the SMM can be condensed into a single calibration constant and that the sample doping is obtained by using a simple analytical formula. © *2010 American Institute of Physics*. [doi:10.1063/1.3482065]

## I. INTRODUCTION

Atomic force microscopy (AFM) related techniques are nowadays used in a wide area of applications ranging from basic research to industrial quality control. Among all these techniques, AFM with conducting tips[1,2] is especially helpful for the investigation of semiconductor nanostructures as well for the local characterization of dielectric layers.[3–5]

The AFM method we want to discuss in this paper is scanning capacitance microscopy/spectroscopy (SCM/SCS) employing microwave reflection techniques, which recently became popular under the name of "scanning microwave microscopy" (SMM). In conventional SCM, a conductive AFM tip is used to measure the local capacitance between the tip and the sample, in SCS, the capacitance is recorded during a dc voltage sweep to obtain a capacitance versus voltage C(V) curve for further analysis. The most important application of this method is two-dimensional carrier profiling for failure analysis especially on cross sectional samples. In addition to carrier profiling, SCM/SCS can also be used for a analysis of dielectric films such as high-k layers[6,7] on the nanoscale. More information about this topic can be found in the review articles in Refs. 8 and 9, examples.

SMMs now combine the outstanding local resolution of an AFM with microwave signal compatibility.[10–16] Thus, SMMs can be regarded as a kind of "next-generation SCM," however, with much larger flexibility also for nonsemiconductor applications. SMMs integrate microwave signals into standard AFM platforms for a variety of applications, a including broadband characterization of material properties.[17] The microwave integration is typically achieved by incorporating a broadband signal path to the AFM tip, often via a resonant structure such as a microwave cavity resonator. The microwave reflection of the tip-sample system is measured employing a commercially available (Agilent) performance network analyzer (PNA) to achieve stable, repeatable, and traceable measurements of the high frequency signal between 1 and 20 GHz.

In this paper, the principles of capacitance measurements on metal-semiconductor-oxide (MOS) structures by using a SMM (Agilent) are discussed. Simulating the electronic SMM behavior by a LCR equivalent circuit which is detuned by a voltage dependent MOS capacitor, we demonstrate the influence of oxide thickness, tip area, doping, operation frequency, and sample bias. For calibrated doping profiling we show, that under appropriate operation conditions, the sample doping can be obtained through a simple analytical formula with only one universal calibration parameter.

## II. EXPERIMENTAL

Figure 1(a) shows the schematic drawing of the SMM setup. The AFM tip, which is in contact with the sample, is connected to the PNA using a transmission line coaxial resonator with a characteristic impedance of 50 Ω. The microwave signal, generated by the PNA (Agilent N5230C), is applied to the sample and the amount of signal reflected from the sample is dependent on the mismatch between the sample impedance and the transmission line impedance. The mismatch, in turn, depends on the material properties of the sample under investigation, which in our case is the capacitance of the MOS structure underneath the AFM tip. As the sensitivity of this approach is significantly decreased if the sample impedance is too far away from 50 Ω, a 50 Ω shunt resistor, in conjunction with a half-wavelength coaxial resonator, is used.

For SMM measurements, a PNA frequency sweep is carried out first, where the PNA amplitude (which is the microwave scattering parameter $S_{11}$) is plotted as a function of frequency. Figure 1(b) shows a typical sweep curve, where one can see a large number of oscillations on which a series of sharp resonances are superimposed. The low frequency oscillations in this curve are PNA artifacts and could be removed by a PNA calibration procedure, which however was

a)Electronic mail: juergen.smoliner@tuwien.ac.at.

 

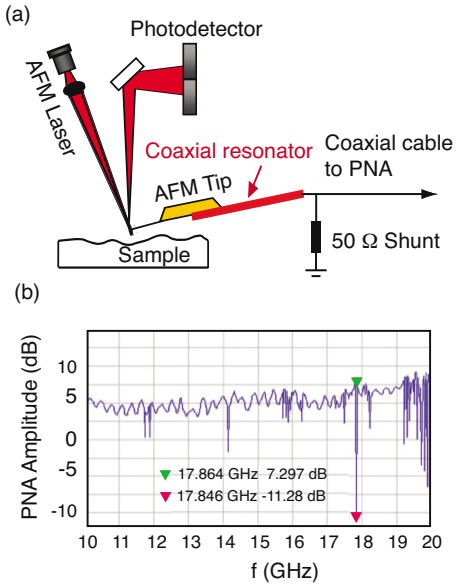


FIG. 1. (Color online) (a) Schematic drawing of the SMM setup. (b) Typical PNA frequency sweep with connected AFM. The resonance, which is used for the measurements is located at f=18 GHz and has a width of 2 ×19 MHz=38 MHz and a depth of ≈18 dB.

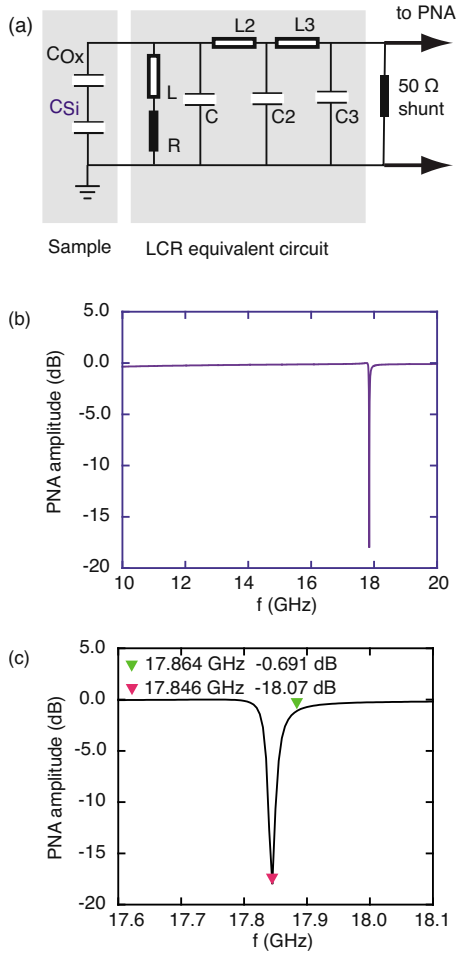


FIG. 2. (Color online) (a) LCR equivalent circuit (sixth order notch filter) used to describe the microwave behavior of the SMM at 17.8 GHz. C =5.2 pF, C2=18.5 fF, C3=50.45 fF. L=0.1 nH, L2=0.092 nH, L3 =1.5 nH, and R=43 Ohm. $C_{ox}$ is the oxide capacitance and the capacitance of the silicon space charge region is $C_{Si}$. (b) Transmission behavior as a function of frequency. (c) Close up of the resonance region.

not yet implemented in the SMM software used. For SMM measurements only the narrow resonances are of importance, since they define the frequencies where SMM measurements can be carried out. After a $S_{11}$ resonance is selected at the desired frequency, any changes in the sample capacitance, e.g., will shift this resonance and thus a change in the measured $S_{11}$ value is detected. The higher the Q-factor ($f_0/\Delta f$) of this resonance, the larger the sensitivity of the measurement will be.

Construction details of the SMM tip-holder or an "official" equivalent circuit of the SMM setup were not available from the manufacturer, but nevertheless, the properties of the coaxial resonator can be described using a simple analytical model. A sixth order equivalent LCR notch filter circuit turned out to be a simple and convenient choice for this purpose, and in this way, a semiquantitative discussion of SMM on MOS structures can be made, which gives a lot of insight into the parameters influencing the SMM measurements. Note, that all the capacitances and inductivities in the equivalent circuit only serve the purpose to reproduce the shape of the measured resonance in our simulation and cannot be associated directly to any hardware components of the SMM.

The LCR filter we used for our simulation is outlined in Fig. 2(a) and consists of mainly three components, the capacitance of the tip-sample system, the LCR circuit describing the properties of the microwave resonator, and the 50 Ω shunt resistor. Calculating the impedance Z of the complete circuit is straightforward and easy, the scattering parameter $S_{11}$ is obtained from the relation: $S_{11}=(Z-50\ \Omega/Z+50\ \Omega)$. As one can see, the calculated sweep curves Figs. 2(b) and 2(c) nicely reproduce the depth and the width (quality factor) of the resonance in the measured PNA frequency sweep at f≈18 GHz. Due to the simplicity of the model, however, only one resonance occurs in the calculated curve. The measured resonances of higher order are not reproduced in the calculated frequency spectrum, and thus, the capacitances and inductivities in the LCR model have to be changed in case a resonance at different frequencies shall be considered.

For the tip-sample contact, a nanoscale, parallel plate MOS capacitor model is used. For the AFM tip we assumed highly doped diamond with a work function of 5.5 eV.[18] For the tip radius we used a typical value of 30 nm, for the oxide we used $Al_2O_3$ (d=3 nm, $\varepsilon_r$=9) like in our previous publications.[19,20] Any oxide charges were neglected. Such a MOS system has a bias and doping dependent capacitance, which we describe using analytic MOS theories from standard textbooks.[21] By changing the tip bias or moving the tip to a position of different doping, the MOS system will detune the LCR circuit, and as a consequence, a change in the PNA amplitude $S_{11}$ and it's derivative $dS_{11}/dV_{tip}$ will be detected.

The most popular application of SCM is the mapping of the carrier concentration in a doped semiconductor sample. For this purpose, the local capacitance between tip (=metal) and sample (semiconductor with thin oxide layer on top) has to be measured. In SMM this is done indirectly by

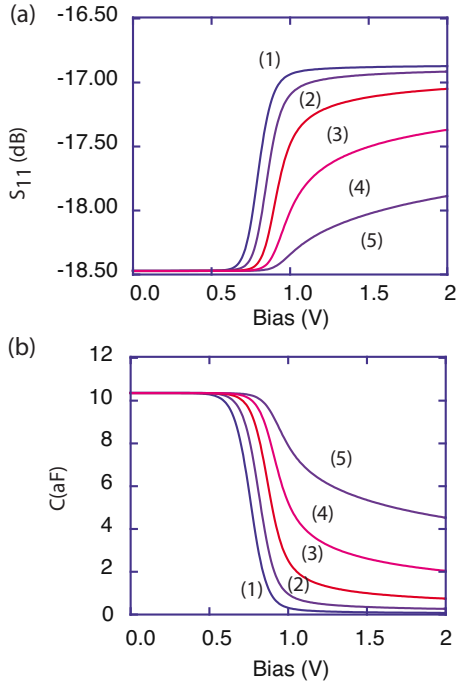


FIG. 3. (Color online) (a): $S_{11}$ (f=18 GHz) calculated as a function of tip bias, for a p-type silicon sample. The curves (1)–(5) represent doping levels of $N_A=1\times10^{15}$ cm$^{-3}$, $N_A=1\times10^{16}$ cm$^{-3}$, $N_A=1\times10^{17}$ cm$^{-3}$, $N_A=1\times10^{18}$ cm$^{-3}$, and $N_A=1\times10^{19}$ cm$^{-3}$, respectively. The tip area was $30\times30$ nm$^2$ and the oxide thickness was 1 nm. (b) Corresponding C(V) curves for the same doping levels.

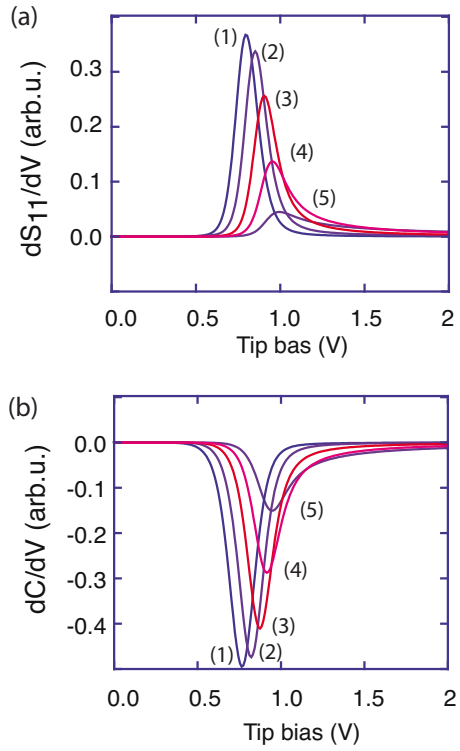


FIG. 4. (Color online) (a) $dS_{11}/dV$ calculated as a function of tip bias, for a p-type silicon sample. The various curves represent doping levels between $N_A=1\times10^{15}$, $1\times10^{16}$, $1\times10^{17}$, $1\times10^{18}$, and $1\times10^{19}$ cm$^{-3}$. The largest signal belongs to the lowest doping level (f=18 GHz). (b) Corresponding dC/dV curves.

measuring $S_{11}$ and converting it into a capacitance value, which, however, is not a disadvantage. In practice, not $S_{11}$ will be measured to determine the local doping levels, but $dS_{11}/dV_{tip}$ since it yields larger sensitivity and a larger signal to noise ratio by using lock-in amplifiers. The latter is essential for acceptable data acquisition times in SMM imaging. The conversion of SMM data into doping profiles, however, is not straightforward. In addition to the well know problems in SCM, the features and properties of the SMM microwave circuitry have to be understood. For this purpose, our semiquantitative model was developed, the results of which are outlined below. Tip geometry effects, however, were not included in our considerations.

## III. RESULTS AND DISCUSSION

The starting point of every SMM measurement is the choice of a suitable resonance position for operation at the desired frequency. For our simulation, the chosen resonance frequency was 18 GHz, the frequency offset from the resonance frequency was 10 MHz. This relatively large offset was chosen intentionally to guarantee numerical stability in our simulation for those cases, where other parameters than the tip bias are varied. The problems related to the proper choice of this frequency offset will be discussed later.

After the resonance position is chosen, the scattering parameter $S_{11}$ can be calculated as a function of sample bias and doping as it is shown in Fig. 3(a). For the calculation, we assumed a p-type silicon sample with doping levels of $N_A=1\times10^{15}$ cm$^{-3}$, $N_A=1\times10^{16}$ cm$^{-3}$, $N_A=1\times10^{17}$ cm$^{-3}$, $N_A=1\times10^{18}$ cm$^{-3}$, and $N_A=1\times10^{19}$ cm$^{-3}$, respectively [curves (1)–(5)]. In Fig. 3(b) the corresponding C(V) curves are shown for comparison. As one can see, the $S_{11}$ curves reflect the shape of the C(V) curve of a MOS system but they are flipped with respect to the $V_{Tip}=1$ V position. Furthermore, it is obvious that the change in the $S_{11}$ signal with sample bias is quite small. For practical purposes, $dS_{11}/dV$ measurements are, therefore, preferred, which are much more sensitive because lock-in amplifiers can be used.

Figure 4(a) shows the derivative $dS_{11}/dV$ calculated as a function of tip bias for a p-type silicon sample. Like above, curves (1)–(5) represent doping levels between $N_A=1\times10^{15}$ and $1\times10^{19}$ cm$^{-3}$. The largest signal belongs to the lowest doping. For comparison, Fig. 4(b) shows the corresponding dC/dV curves, which look quite similar. The sign of the dC/dV curves, however is inverted compared to the $dS_{11}/dV$ curves.

To convert SMM data into doping maps so called "calibration curves" have to be calculated, which are the relation between the actual $dS_{11}/dV$ value and the corresponding doping level. These calibration curves, however, depend on a number of parameters, which will be discussed in the following. Note, that in all following experimental considerations, the ac modulation voltage, (ac drive amplitude on the Agilent SMM) which is required to measure $dS_{11}/dV$ using a lock-in amplifier, is assumed to be as small as possible, otherwise the calibration curves are severely distorted.

Figure 5(a) shows four typical calibration curves calculated for four different tip bias values. All parameters for this calculation are the same like for the previous figures. Below tip bias values of $V_{Tip}\approx0.7$ V all these calibration curves

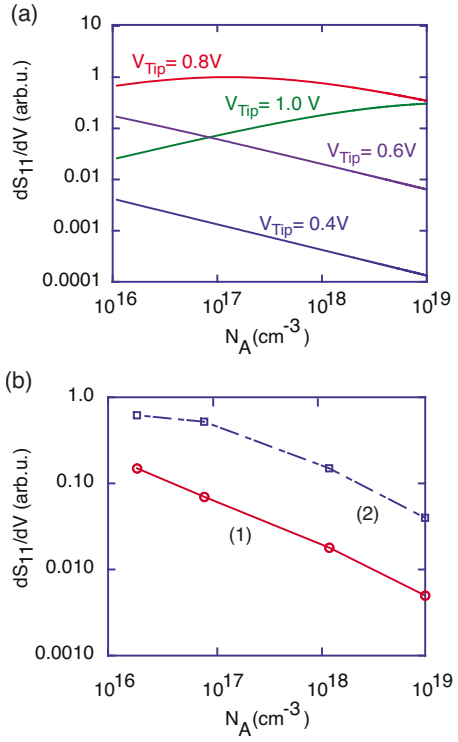


FIG. 5. (Color online) (a) Calibration curves calculated for various bias values around the position of the largest signal (V=+0.6 V). For this calculation, the value of f was f=18 GHz, the oxide thickness was 1 nm. Frequency offset 10 MHz. (b) Experimentally measured calibration curves.

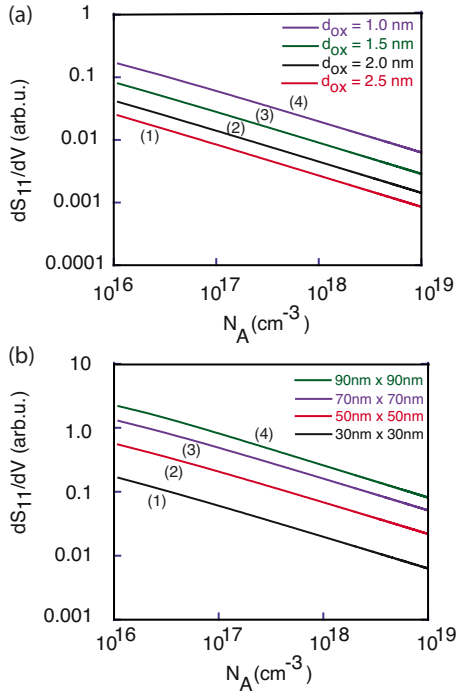


FIG. 6. (Color online) (a) Calibration curves (18 GHz) with oxide thickness as parameter. Curves (1)–(4) correspond to an oxide thickness of 2.5 nm, 2 nm, 1.5 nm, and 1 nm, respectively. For this calculation, the tip area was $30\times30$ nm$^2$ and $V_{Tip}=0.6$ V. (b) Calibration curves for AFM Tip areas of $30\times30$ nm$^2$, $50\times50$ nm$^2$, $70\times70$ nm$^2$, and $90\times90$ nm$^2$, [curves (1)–(4)], respectively. ($d_{ox}=1$ nm and $V_{Tip}=0.6$ V).

are linear and parallel on a double logarithmic scale. At $V_{Tip}\approx+0.8$ V the signal is largest but the calibration curve becomes nonlinear. For values of $V_{Tip}=1$ V and larger, the calibration curve gets the opposite slope and gets smaller in total. For direct comparison, Fig. 5(b) shows measured calibration curves, which were obtained on p-type silicon doping staircase, which was provided by IMEC, Belgium. Curve (1) was measured at a bias of $V_{Tip}=-0.5$ V, curve (2) at $V_{Tip}=-0.8$ V. As one can see, curve (1) nicely matches the behavior of the calculated curve at $V_{Tip}\approx+0.6$ V, curve (2) corresponds to the calculated curve at $V_{Tip}\approx+0.8$ V. Compared to the calculated curves, the experimental curves are shifted to more negative bias. This, however, is due to the fact that for the experiments solid platinum tips were used (Rocky Mountain Nanotechnology), which has a different work function compared to diamond used in our simulation. Further, oxide charges were also neglected for our simulation.

The strong bias dependence of the calibration curves has a very important consequence, namely, that the relation between doping and SMM signal is not necessarily monotonic if improper tip bias values are chosen. Only if it is made sure, that tip-sample system is in "accumulation" conditions for all doping levels present on the investigated sample, the calibration curves will be monotonic, linear and parallel on a double logarithmic scale. For p-type samples this means, that the tip bias $V_{Tip}$ has to be adjusted in a way, that the bias point of SMM operation is always on the left side of the dC/dV peak for all doping levels, which are present on the investigated sample (see Fig. 4). For n-type samples, the identical arguments apply but the signs of all bias scales have to be reversed. Finally, it must be pointed out, that In the vicinity of pn-junctions, all above arguments are no longer valid.

We now study the influence of oxide thickness on the SMM signal. Figure 6(a) shows four calibration curves for a oxide thickness of 1 nm, 1.5 nm, 2 nm, and 2.5 nm, [curves (1)–(4)] respectively. As one can see, the calibration curves are linear and parallel and the signal size decreases approximately by a factor of 10 if the oxide thickness increases from $d_{Ox}=1$ to 2 nm. Thus, thin oxides should be used for SMM. Note, that thick oxides will also reduce the spatial resolution of the measurement.

The tip area also has a strong influence on the calibration curves. Figure 6(b) shows calibration curves for a tip areas of $30\times30$ nm$^2$, $50\times50$ nm$^2$, $70\times60$ nm$^2$, and $90\times90$ nm$^2$, respectively [curves (1)–(4)]. For larger areas, the signal becomes larger. As in Fig. 6(a), the calibration curves stay linear and are parallel if the tip area is increased. The rate at which the signal increases with increasing tip area is not linear.

Another important point is the influence of the operation frequency on the calibration curves. Figure 7 shows the calibration curves calculated for 5, 10, and 18 GHz, the quality factors of the corresponding resonances are 500 at 18 GHz, 41 at 10 GHz, and 1.2 at 5 GHz, respectively. The calculated $dS_{11}/dV$ values become larger for higher frequencies, (or in other words higher quality factors), which is also found experimentally.

Concerning the operation frequency, there is one point, which must be discussed in greater detail: for proper SMM

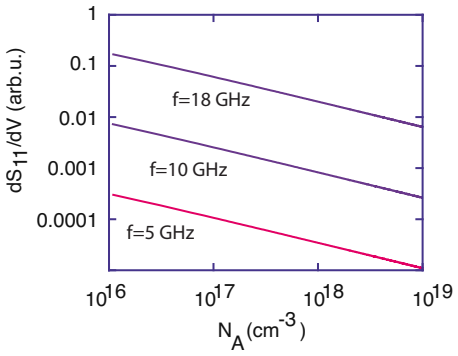


FIG. 7. (Color online) Calibration curves calculated for three different frequencies. The quality factors of the resonances are 500 at $f_0=18$ GHz, 41 at $f_0=10$ GHz and 1.2 at $f_0=5$ GHz, respectively. ($V_{Tip}=0.6$ V, $d_{ox}=1$ nm, and tip area $30\times30$ nm$^2$).

operation, the frequency is not chosen at the resonance position, but at a certain positive or negative offset with respect to the resonance frequency. The choice of this offset can be somewhat critical as we will show below.

In Fig. 8(a) we have plotted $S_{11}(V)$ for different frequency offsets from the resonance position at $f_0=18$ GHz. The respective d $S_{11}/dV$ curves are shown in Fig. 8(b). The curves were calculated for frequency offsets of 3 MHz, 5 MHz, 10 MHz, and 15 MHz, respectively. The largest signal is obtained for the smallest frequency offset. For larger offsets, the signals become quite small very quickly. Note that in case a neighbored resonance is unintentionally reached, the signal will become inverted.

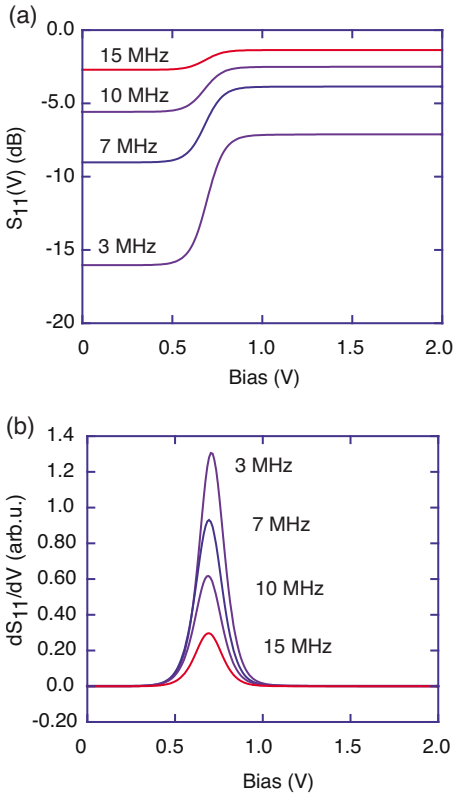


FIG. 8. (Color online) (a) $S_{11}(V)$ curves and their respective derivatives (b) measured as a function of the frequency offset from the resonance position $f_0=18$ GHz. The doping was $N_A=1\times10^{16}$ cm$^{-3}$. The shown curves were calculated for frequency offsets of 3 MHz, 5 MHz, 10 MHz, and 15 MHz, respectively.

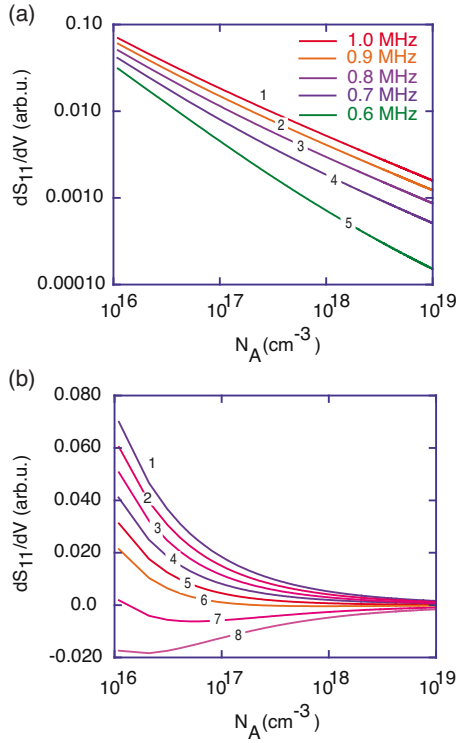


FIG. 9. (Color online) (a) Calibration curves for frequency offsets between 1 to 0.6 MHz is steps of 0.1 MHz. Tip area 30 nm$\times$30 nm, $N_A=1\times10^{15}$ cm$^{-3}$, $f_0=18$ GHz, and $V_{Tip}=0.6$ V. (b) Calibration curves on a linear scale for frequency offsets in the range between 1 MHz [curve (1)] and 0.3 MHz [curve (8)].

Although Fig. 8 suggests, that one should go as close as possible to the resonance position for maximum signal size, this is not a good idea. To illustrate this with an example, we consider the case of different doping levels inside the investigated sample: Any change in sample doping will detune the LCR circuit, but it is not clear, whether the resonance will be shifted to higher or lower frequencies and to which amount. Under unfavorable circumstances it can therefore happen, that the working point is moved to the other side of $f_0$. In this case, the calibration curve can behave quite unexpected.

Figure 9 illustrates the effects, which can occur in case the frequency offset becomes too small. The shown calibration curves were calculated at a frequency of 18 GHz and frequency offsets ranging from 1 to 0.6 MHz is steps of 0.1 MHz. As one can see clearly, the calibration curves are no longer parallel when the frequency offset becomes smaller. For lower frequency offsets (and plotted on linear scales), this effect becomes even more pronounced. At 0.3 MHz, $dS_{11}/dV$ is already negative, and thus, the calibration curves are no longer useful. For this reason it will be wise to stay a safe distance away from the resonance position in a real world experiment. According to our simulations, a frequency around the "full width half maximum" of the resonance is the most robust choice for SMM measurements. In addition, this choice has the advantage, that the derivative of the resonance curve has its maximum at this position and therefore the sensitivity is largest.

Looking at all the plots above, which show the dependencies of the calibration curves on the various discussed parameters, it is very conspicuous, that on double logarith-

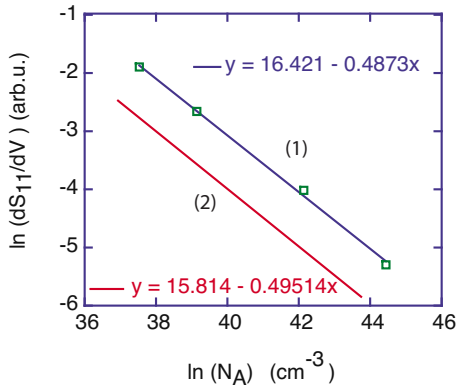


FIG. 10. (Color online) Measured [curve (1)] and calculated [curve (2)] calibration curves on natural log-scales. For the calculation, the parameters are identical with Fig. 6(a), curve 3 ($f_0$=18 GHz, $V_{Tip}$=0.6 V, $d_{ox}$ =1.5 nm, and tip area $30\times30$ nm$^2$). As one can see from the linear fits in the plot, the slope is almost perfectly −0.5 both for the calculation and the experiment.

mic scales the calibration curves are all parallel and moreover, they always have the same slope independent, which parameter is varied. This strange behavior becomes more clear, if one changes the plot scales from $\log_{10}$ to the natural logarithm, "ln." As typical example we have plotted the calibration curve (3) from Fig. 6(a) and typical experimental data on natural log-scales in Fig. 10. A linear fit to the data is also shown. On natural log-scales, the slope of both curves is almost exactly −0.5, which can be understood, however, by textbook MOS theory. The factor "−0.5" simply reflects the fact that the thickness of space charge region in the silicon sample is inverse proportional to the square root of the doping level. This behavior is then linearly translated into the SMM signals, however, only if proper operating parameters and small signal conditions (i.e., a sufficiently small modulation voltage for the $dS_{11}/dV$ measurement) are used.

The above finding, that on double logarithmic scales all calibration curves are parallel and always have the same slope, independent, which experimental parameter is varied can be expressed in terms of a "golden calibration rule" for SMM on doped semiconductors

$$\ln(dS_{11}/dV) = -0.5\ln(N_A) + K_{calib}, \quad (1)$$

where all experimental parameters can be summarized into a single calibration constant ($K_{calib}$). Note, however, that due to the difference in the density of states, $K_{calib}$ is different in p-type and n-type samples, even if all other parameters are the same.

Equation (1) also shows the main strength of SMM for doping profiling on semiconductors. To determine $K_{calib}$ for a quantitative determination of local doping levels only one calibration point is required, either on the sample under investigation, where the known substrate doping can be exploited, e.g., or on a reference sample with known doping level and the same oxide thickness than the sample under investigation. It must be pointed out, that quantitative SCM measurements like in Ref. 18 are not of advantage compared to SMM. To determine doping levels by quantitative SCM, the tip area has to be determined first and, moreover, a parasitic background capacitance has always to be subtracted. For precise measurements, once again a calibration sample is required, and thus, the number of calibration constants in quantitative SCM is even larger than in SMM. Finally, quantitative low frequency SCM measurements are extremely time consuming. At comparable signal to noise ratio, the data acquisition times for low frequency capacitance spectra (1 kHz) is easily in the order of 24 h, whereas calibrated dC/dV spectra can be measured in seconds by SMM at comparable spectral resolution. A detailed analysis of the technical SMM performance will be subject of further investigations, but the model calculations presented in this paper already indicate, that SMM is a very promising development for doping profiling on semiconductors and other applications.

## IV. SUMMARY

In summary, an analytical model of SMM was developed. The model was applied to SMM on semiconductor samples incorporating the tip-sample interactions by the physics of MOS junctions. It was shown that a quantitative determination of doping levels by SMM is possible using a simple analytic relation, in which a single calibration constant includes all relevant operation parameters of the SMM. The critical parameters, which can lead to a breakdown of the simple model, are essentially the tip bias $V_{Tip}$ and the frequency offset from the resonance $f_0$ at which the SMM is operated. The influence of these critical parameters was discussed in detail.

## ACKNOWLEDGMENTS

This work was sponsored by the NSI-Nanoshape-II Project, (Nano Initiative Austria, Project No. V110-08BI) and by FWF-Austria, Project No. SFB-25-08 (IR-ON) and the Christian Doppler Society.

[1] I. Tanaka, I. Kamiya, H. Sakaki, N. Qureshi, S. J. Allen, Jr., and P. M. Petroff, Appl. Phys. Lett. **74**, 844 (1999).
[2] I. Tanaka, E. Kawasaki, O. Ohtsuki, K. Uno, M. Hara, H. Asami, and I. Kamiya, Surf. Sci. **532–535**, 801 (2003).
[3] X. Blasco, M. Nafria, X. Aymerich, and W. Vandervorst, Electron. Lett. **41**, 719 (2005).
[4] C. Sire, S. Blonkowski, M. J. Gordon, and T. Baron, Appl. Phys. Lett. **91**, 242905 (2007).
[5] S. Kremmer, C. Teichert, E. Pischler, H. Gold, K. Kuchar, and M. Schatzmayr, Surf. Interface Anal. **33**, 168 (2002).
[6] W. Brezna, S. Harasek, H. Enichlmair, E. Bertagnolli, E. Gornik, and J. Smoliner, J. Appl. Phys. **92**, 2144 (2002).
[7] W. Brezna, S. Harasek, A. Lugstein, T. Leitner, H. Hoffmann, E. Bertagnolli, and J. Smoliner, J. Appl. Phys. **97**, 093701 (2005).
[8] V. V. Zavyalov, J. S. McMurray, and C. C. Williams, Rev. Sci. Instrum. **70**, 158 (1999).
[9] P. De Wolf, R. Stephenson, T. Trenkler, T. Clarysse, T. Hantschel, and W. Vandervorst, J. Vac. Sci. Technol. B **18**, 361 (2000).
[10] B. T. Rosner and D. W. van der Weide, Rev. Sci. Instrum. **73**, 2505 (2002).
[11] C. Gao and X.-D. Xiang, Rev. Sci. Instrum. **69**, 3846 (1998).
[12] V. V. Talanov, A. Scherz, R. L. Moreland, and A. R. Schwartz, Appl. Phys. Lett. **88**, 134106 (2006).
[13] J. Kim, K. Lee, B. Friedman, and D. Cha, Appl. Phys. Lett. **83**, 1032 (2003).
[14] M. Tabib-Azar, D. P. Su, and A. Pohar, Rev. Sci. Instrum. **70**, 1725 (1999).
[15] A. Imtiaz, S. M. Anlage, J. D. Barry, and J. Melngailis, Appl. Phys. Lett. **90**, 143106 (2007).
[16] A. Imtiaz and S. M. Anlage, Ultramicroscopy **94**, 209 (2003).
[17] S. M. Anlage, V. V. Talanov, and A. R. Schwartz, in *Scanning Probe Microscopy: Electrical and Electromechanical Phenomena at the Nano-*

*scale*, edited by S. Kalinin and A. Gruverman (Springer, New York, 2007), 1, 215.
[18]W. Brezna, M. Schramboeck, A. Lugstein, S. Harasek, H. Enichlmair, E. Bertagnolli, E. Gornik, and J. Smoliner, Appl. Phys. Lett. **83**, 4253 (2003).
[19]C. Eckhardt, W. Brezna, O. Bethge, E. Bertagnolli, and J. Smoliner, J. Appl. Phys. **105**, 113709 (2009).
[20]C. Eckhardt, J. Silvano, W. Brezna, O. Bethge, E. Bertagnolli, and J. Smoliner, J. Appl. Phys. **107**, 064320 (2010).
[21]S. M. Sze, *The Physics of Semiconductor Devices* (Wiley-Interscience, New York, 1981).